

Two-dimensional heavy fermions in the van der Waals metal CeSil

<https://doi.org/10.1038/s41586-023-06868-x>

Received: 26 January 2023

Accepted: 14 November 2023

Published online: 17 January 2024

 Check for updates

Victoria A. Posey¹, Simon Turkel^{2,3,16}, Mehdi Rezaee^{4,16}, Aravind Devarakonda^{2,16}, Asish K. Kundu^{3,16}, Chin Shen Ong^{5,16}, Morgan Thinel^{1,2}, Daniel G. Chica¹, Rocco A. Vitalone², Ran Jing², Suheng Xu², David R. Needell¹, Elena Meirzadeh¹, Margalit L. Feuer¹, Apoorv Jindal², Xiaomeng Cui⁴, Tonica Valla^{3,6}, Patrik Thunström⁵, Turgut Yilmaz⁷, Elio Vescovo⁷, David Graf⁸, Xiaoyang Zhu¹, Allen Scheie^{9,10}, Andrew F. May¹¹, Olle Eriksson^{5,12}, D. N. Basov², Cory R. Dean², Angel Rubio^{13,14,15}, Philip Kim⁴, Michael E. Ziebell¹¹, Andrew J. Millis^{2,15}, Abhay N. Pasupathy^{2,3} & Xavier Roy¹

Heavy-fermion metals are prototype systems for observing emergent quantum phases driven by electronic interactions^{1–6}. A long-standing aspiration is the dimensional reduction of these materials to exert control over their quantum phases^{7–11}, which remains a significant challenge because traditional intermetallic heavy-fermion compounds have three-dimensional atomic and electronic structures. Here we report comprehensive thermodynamic and spectroscopic evidence of an antiferromagnetically ordered heavy-fermion ground state in CeSil, an intermetallic comprising two-dimensional (2D) metallic sheets held together by weak interlayer van der Waals (vdW) interactions. Owing to its vdW nature, CeSil has a quasi-2D electronic structure, and we can control its physical dimension through exfoliation. The emergence of coherent hybridization of *f* and conduction electrons at low temperature is supported by the temperature evolution of angle-resolved photoemission and scanning tunnelling spectra near the Fermi level and by heat capacity measurements. Electrical transport measurements on few-layer flakes reveal heavy-fermion behaviour and magnetic order down to the ultra-thin regime. Our work establishes CeSil and related materials as a unique platform for studying dimensionally confined heavy fermions in bulk crystals and employing 2D device fabrication techniques and vdW heterostructures¹² to manipulate the interplay between Kondo screening, magnetic order and proximity effects.

One strategy for creating strongly correlated materials is to design intermetallic compounds with lattices of localized magnetic moments (typically Ce, Yb or U) that can hybridize with itinerant electrons to produce an emergent, narrow band of heavy fermions^{5,13–15}. The interplay¹⁴ between the Kondo effect, which screens local moments to create a heavy-fermion state, and intersite exchange interactions, typically of Ruderman–Kittel–Kasuya–Yosida form, which induce magnetic ordering, produces a variety of emergent quantum phenomena, including heavy Fermi liquids¹⁶; magnetic, orbital and hidden order states^{3,4}; unconventional superconductivity¹⁶ and quantum criticality^{2,17}. In conventional intermetallic heavy-fermion materials, this interplay is tuned using external parameters, such as pressure^{17,18}, chemical doping¹⁹, magnetic fields²⁰ and, more recently, dimensionality²¹. Bulk crystals^{22–24}

and epitaxial superlattices^{7,8,25,26} hosting quasi-two-dimensional (2D) electronic and magnetic structures display reduced Kondo screening and enhanced quantum fluctuations compared to their three-dimensional counterparts, motivating the discovery of materials that can be used to study Kondo physics at the monolayer limit.

van der Waals (vdW) heavy-fermion metals offer new opportunities to access 2D electronic states in which quantum confinement or anisotropic interactions yield enhanced correlations²⁷ and new quantum phases^{17,22,28}. The exfoliation of these vdW crystals is expected to strengthen long-range Coulomb interactions at the 2D limit and enable fabrication of gateable devices^{11,12} and heterostructures¹², opening possibilities for controlling emergent quantum phenomena. To date, however, there are no examples of a vdW metal with an unambiguous

¹Chemistry Department, Columbia University, New York, NY, USA. ²Physics Department, Columbia University, New York, NY, USA. ³Condensed Matter Physics and Materials Science Division, Brookhaven National Laboratory, Upton, NY, USA. ⁴Physics Department, Harvard University, Cambridge, MA, USA. ⁵Department of Physics and Astronomy, Uppsala University, Uppsala, Sweden.

⁶Donostia International Physics Center (DIPC), Donostia-San Sebastián, Spain. ⁷National Synchrotron Light Source II, Brookhaven National Lab, Upton, NY, USA. ⁸National High Magnetic Field Laboratory, Florida State University, Tallahassee, FL, USA. ⁹Neutron Scattering Division, Oak Ridge National Lab, Oak Ridge, TN, USA. ¹⁰MPA-Q, Los Alamos National Lab, Los Alamos, NM, USA.

¹¹Materials Science and Technology Division, Oak Ridge National Lab, Oak Ridge, TN, USA. ¹²Wallenberg Initiative Materials Science for Sustainability, Uppsala University, Uppsala, Sweden.

¹³Max Planck Institute for the Structure and Dynamics of Matter, Center for Free-Electron Laser Science and Department of Physics, Hamburg, Germany. ¹⁴Nano-Bio Spectroscopy Group and European Theoretical Spectroscopy Facility (ETSF), Departamento de Polímeros y Materiales Avanzados: Física, Química y Tecnología, Universidad del País Vasco (UPV/EHU), San Sebastián, Spain. ¹⁵Center for Computational Quantum Physics, Flatiron Institute, New York, NY, USA. ¹⁶These authors contributed equally: Simon Turkel, Mehdi Rezaee, Aravind Devarakonda, Asish K. Kundu, Chin Shen Ong. [✉]e-mail: angel.rubio@mpsd.mpg.de; mez2127@columbia.edu; ajm2010@columbia.edu; apn2108@columbia.edu; xr2114@columbia.edu

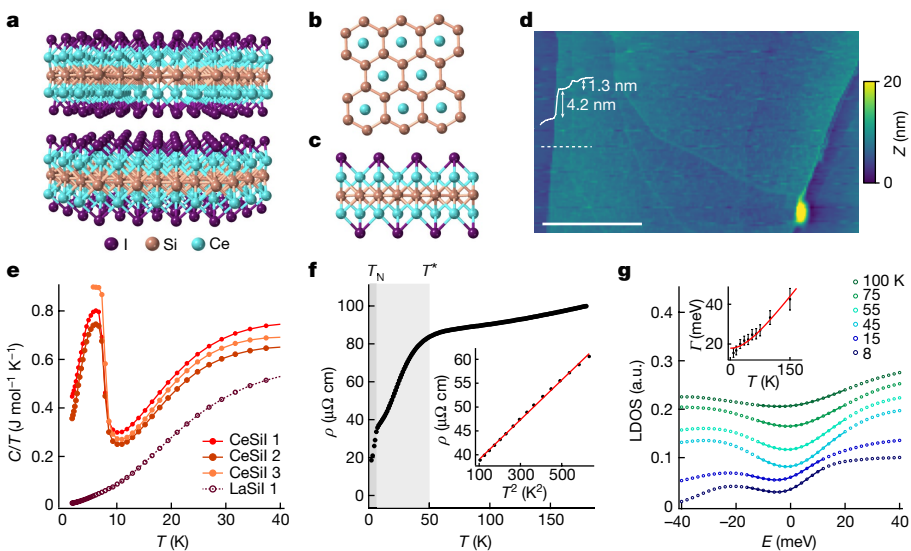


Fig. 1 | Crystal structure, exfoliation and heavy-fermion behaviour of CeSil.

a, Crystal structure of CeSil. **b**, Top view of the silicene-like layer with the iodine atoms removed for clarity. **c**, Side view of a single CeSil layer. **d**, Atomic force microscopy image and height profile (along the white dashed line) of a mechanically exfoliated ultra-thin flake of CeSil on a Si/Si₃N₄ wafer. The 4.2 nm step height is consistent with a trilayer flake with the subsequent 1.3 nm step corresponding to one additional layer. Scale bar, 5 μm. **e**, Temperature dependence of the heat capacity for several samples. **f**, Temperature dependence of the resistivity at zero magnetic field, with the darker grey region indicating the AFM phase and the lighter grey denoting the coherence regime. Inset,

resistivity as a function of T^2 in the Kondo-lattice regime ($10 \text{ K} < T < 25 \text{ K}$), with the Fermi liquid linear fit as the red line. **g**, Local density of states (LDOS) of CeSil from $T = 8$ to 100 K. Each temperature was fitted using a spectral Fano function shown by the solid line. Each spectrum is the average of 200 spectra taken with the same setpoint ($I = 150 \text{ pA}$, $V = 100 \text{ meV}$) and a 2 meV lock-in modulation. Spectra are offset for clarity. The rest of the temperature-dependent data can be found in Extended Data Fig. 4. Inset, temperature dependence of the Fano width (Γ) extracted from the fits. The red line represents the temperature dependence for a single Kondo impurity. a.u., arbitrary units.

heavy-fermion ground state. The vdW metal CeTe₃ shows evidence of Kondo coupling but in the weak coupling regime^{29,30}. Certain vdW heterostructures host ‘artificial’ heavy fermions^{10,31,32}; however, these systems lack the on-site coupling and orbital degeneracy of the correlated sites characteristic of conventional heavy-fermion systems. In our search for a new vdW heavy-fermion material, we identified CeSil as a promising candidate based on its electron itinerancy, as implied by the Zintl–Klemm formalism³³, and the ease of exfoliation and 2D electronic properties implied by its vdW structure.

We synthesized single crystals of CeSil from the high-temperature reaction of Ce, Si and CeI₃ (ref. 33). CeSil grows as thin, hexagonal plate-like crystals with a metallic lustre (Methods). A vdW layer of CeSil (Fig. 1a) consists of a nearly flat 2D honeycomb of Si sandwiched between triangular layers of Ce atoms (Fig. 1b) and capped by iodine atoms (Fig. 1c). Owing to its vdW nature, CeSil can be mechanically exfoliated using standard methods¹², routinely producing atomically thin, micrometre-scale flakes (Fig. 1d).

Signatures of heavy fermions

Preliminary evidence for electronic correlations in CeSil is seen when comparing its Sommerfeld coefficient (γ), which is extracted from the temperature dependence of the heat capacity $C(T)$ (ref. 5; Fig. 1e) and is proportional to the electronic effective mass in Fermi liquid theory³⁴, to that of the non-magnetic, isostructural compound LaSil (Extended Data Fig. 1). CeSil displays a distinct λ-type anomaly at approximately 7 K, attributed to the onset of antiferromagnetic (AFM) ordering, and a Schottky-like anomaly centred at approximately 23 K (Extended Data Fig. 2), ascribed to crystal electric field (CEF) effects. We calculate $\gamma_{\text{CeSil}} = 0.125(54) \text{ J mol}^{-1} \text{ K}^{-2}$ by fitting the total $C(T)/T$ using contributions from LaSil, a CEF model and a Sommerfeld function (Methods and Extended Data Fig. 3). The large enhancement of γ_{CeSil} compared to γ_{LaSil} ($0.003(1) \text{ J mol}^{-1} \text{ K}^{-2}$) is characteristic of moderate correlations. Short-range magnetic interactions or magnetic frustration

probably contribute to the enhanced γ_{CeSil} (ref. 35), but transport and spectroscopic data discussed below imply that hybridization between conduction and 4f electrons (c-f hybridization) largely explains this enhancement. Consistent with this interpretation, γ_{CeSil} is aligned with that of other local-moment, heavy-fermion antiferromagnets^{36,37}.

The temperature dependence of the resistivity $\rho(T)$ provides evidence that Kondo coupling, rather than magnetic interactions, engenders strong correlations in CeSil. When cooling from room temperature, $\rho(T)$ decreases only slightly before a pronounced drop below $T^* \approx 50 \text{ K}$ and a sharper downturn at approximately 7 K (Fig. 1f). Although the low-temperature kink corresponds to the AFM transition seen in $C(T)$, the feature around T^* is a signature of the crossover from incoherent Kondo scattering to heavy-electron Bloch states^{5,13}. In this Kondo-lattice regime, CeSil displays Fermi liquid behaviour (Fig. 1f, inset). Although T^* is broadly aligned with the Schottky anomaly arising from CEF effects in $C(T)$, the depopulation of CEF excited states typically leads to only a weak downturn in $\rho(T)$. The pronounced drop at T^* in CeSil more probably arises from an interplay between Kondo hybridization and CEF effects³⁸. Our temperature-dependent scanning tunnelling spectroscopy (STS) measurements uncovered the strength of this Kondo coupling. At low temperature, the scanning tunnelling spectrum of CeSil shows a dip in the local density of states around the Fermi energy (E_F), which can be fitted to a Fano line shape (Fig. 1g). Given that this spectral feature is not present in LaSil (Extended Data Fig. 4a), we assign it to a Kondo resonance, paralleling previous STS studies of heavy-fermion materials^{39,40}. Fitting the temperature dependence of the Fano linewidth to the single-impurity Kondo model yields a Kondo temperature $T_K = 74(3) \text{ K}$ (Fig. 1g, inset). Similar scaling between T_K and T^* is seen in CeCoIn₅ and URu₂Si₂ (refs. 39,40).

To further substantiate Kondo physics and c-f hybridization, we performed angle-resolved photoemission spectroscopy (ARPES) measurements on LaSil and CeSil. Beyond the nearly identical dispersive bands observed in both materials, ARPES uncovers flat bands in CeSil at $(E - E_F) \approx -0.01$ and -0.27 eV (Fig. 2a), which appear as well-defined

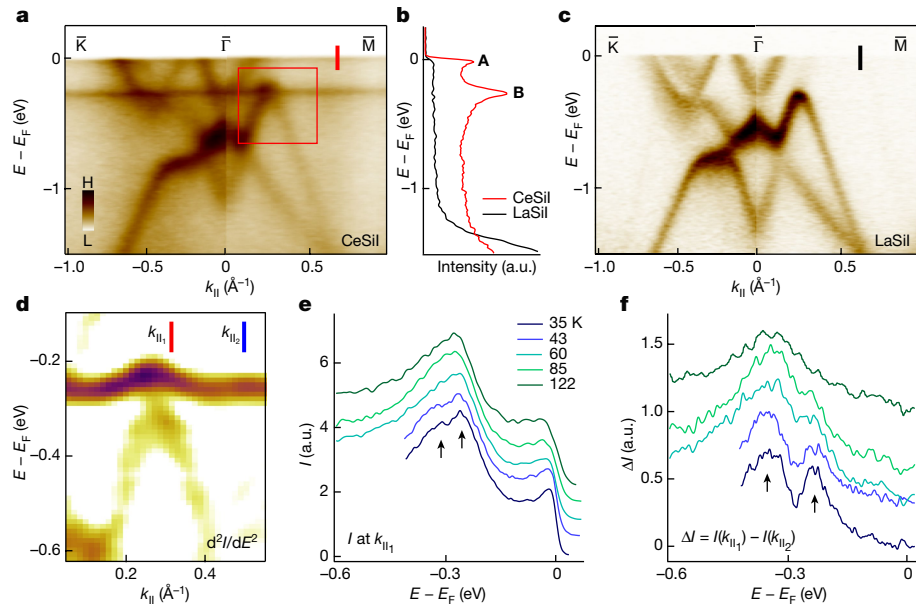


Fig. 2 | Kondo hybridization in ARPES. **a**, ARPES intensity map along the \bar{K} – $\bar{\Gamma}$ – \bar{M} path measured at $T=10$ K using a photon energy of 135 eV for CeSiL. The red box highlights an avoided crossing between the conduction and f bands. **b**, Energy distribution curves for CeSiL and LaSiL integrated along the red and black vertical lines between $\bar{\Gamma}$ and \bar{M} shown in **a** and **c**. The labels **A** and **B** correspond to the Kondo resonance feature and the spin-orbit shake-off feature, respectively. **c**, ARPES spectrum of LaSiL measured using a photon energy of 135 eV at $T=35$ K. **d**, Second derivative of the ARPES intensity (I) (with respect to the energy direction) (d^2I/dE^2) within the region enclosed by

the red box in **a**, showing the hybridization. **e**, Energy distribution curves along k_{\parallel} in **d** at different temperatures measured using a photon energy of 121 eV. **f**, Difference between the intensities along $k_{\parallel 1}$ and $k_{\parallel 2}$ (at and away from the intersection of the dispersive band and the spin-orbit shake-off feature, respectively) shown in **d**, $\Delta I = I(k_{\parallel 1}) - I(k_{\parallel 2})$, for each temperature. The intensities were normalized near E_F before ΔI was calculated. The opening of the hybridization gap results in two peaks, as indicated by the arrows in the data in **e** and **f**.

peaks in the angle-integrated energy distribution curve (Fig. 2b). Because these peaks are absent in the spectrum of $4f^0$ LaSiL (Fig. 2c), we conclude that they originate from Ce $4f^1$ states^{41,42}. We assign the peak at E_F as a Kondo resonance and the peak at -0.27 eV as a spin-orbit shake-off feature⁴³. For CeSiL, Kondo hybridization leading to the formation of heavy fermions manifests as avoided crossings at the intersections of dispersive and flat bands (Fig. 2d and Extended Data Fig. 4c). This hybridization induces a double-peak feature centred at $(E - E_F) \approx -0.3$ eV in the low-temperature energy distribution curve (Fig. 2e), corresponding to a hybridization-induced gap opening at the intersection of the dispersive band and the spin-orbit shake-off feature. The difference spectrum (Fig. 2f) between the energy distribution curve at and away from this intersection further clarifies the presence of a hybridization gap. Temperature-dependent ARPES measurements indicate that the quasiparticle coherence of the Kondo resonance weakens with increasing temperature and that the hybridization gap disappears at approximately 85 K, in line with the STS results.

Magnetic order

Having established the presence of heavy fermions and Kondo hybridization in CeSiL, we turn to understanding its magnetic transition. Figure 3a presents the temperature dependence of the magnetic susceptibility (χ) of CeSiL with the magnetic field H applied along the c axis. At high temperature, CeSiL displays Curie–Weiss-like behaviour (Extended Data Fig. 5), whereas a sharp cusp at the Néel temperature $T_N = 7.5$ K signifies the onset of AFM order. The field dependence of the magnetization (M) at 2 K reveals two metamagnetic transitions at $\mu_0 H = 2.3$ and 4.1 T (Fig. 3b), reaching magnetization plateaus of approximately 0.4 and approximately 0.9 μ_b/Ce , respectively (analysis in Methods). These results agree with a recent neutron-scattering investigation that identified incommensurate AFM order in CeSiL (ref. 44). The integration of $C_{\text{mag}}(T)/T$, where C_{mag} is the magnetic contribution to

C_{CeSiL} (Extended Data Fig. 1), yields a recovered entropy of 73% of $R\ln(2)$ at T_N and 100% by approximately 20 K (Extended Data Fig. 2e), confirming a doublet CEF ground state. Preliminary pressure-dependent measurements reveal a small downward shift in T_N (Extended Data Fig. 6), evidencing that CeSiL is near the peak of the AFM dome in the Doniach (Kondo-magnetic) phase diagram⁴⁵.

Scanning tunnelling microscopy (STM) provides further insights into the magnetism of CeSiL. STM imaging of a cleaved crystal (Fig. 3c) reveals modulations of the density of states in the vicinity of surface defects. The Fourier transform of the STM topography near these defects is a proxy for the electronic susceptibility. The Fourier transform of the STM topographies of both CeSiL (Fig. 3c, inset) and LaSiL (Extended Data Fig. 7a) show a prominent peak at $\mathbf{q}_{\text{AFM}} \approx 0.28$ reciprocal lattice units (arrow in Fig. 4e), matching the propagation wavevector seen in neutron diffraction⁴⁴. This peak results from a nesting vector between critical points in the electronic band structures of both materials (Figs. 3d and 4e for CeSiL; Extended Data Fig. 7c for LaSiL), implying Ruderman–Kittel–Kasuya–Yosida interactions mediate incommensurate AFM ordering of the Ce³⁺ moments at this nesting \mathbf{q}_{AFM} vector. Additionally, although the bulk magnetic order is three-dimensional due to interlayer effects, density functional theory (DFT) calculations reveal substantial anisotropy in the magnetic exchange interactions. The calculated ratio of the intralayer nearest-neighbour exchange coupling to the interlayer exchange coupling is greater than 100, compared to approximately 10 in quasi-2D CeRhIn₅ (ref. 46), suggesting that the magnetism of CeSiL is dominated by 2D interactions (extended discussion in Methods).

The magnetic ordering and metamagnetic transitions are evident in the temperature- and angle-dependent magnetotransport of CeSiL. When H is applied along the crystallographic c axis, CeSiL exhibits a large, non-saturating positive magnetoresistance up to at least 31 T (Extended Data Fig. 8a), consistent with the coexistence of several hole and electron Fermi pockets⁴⁷. Both metamagnetic transitions

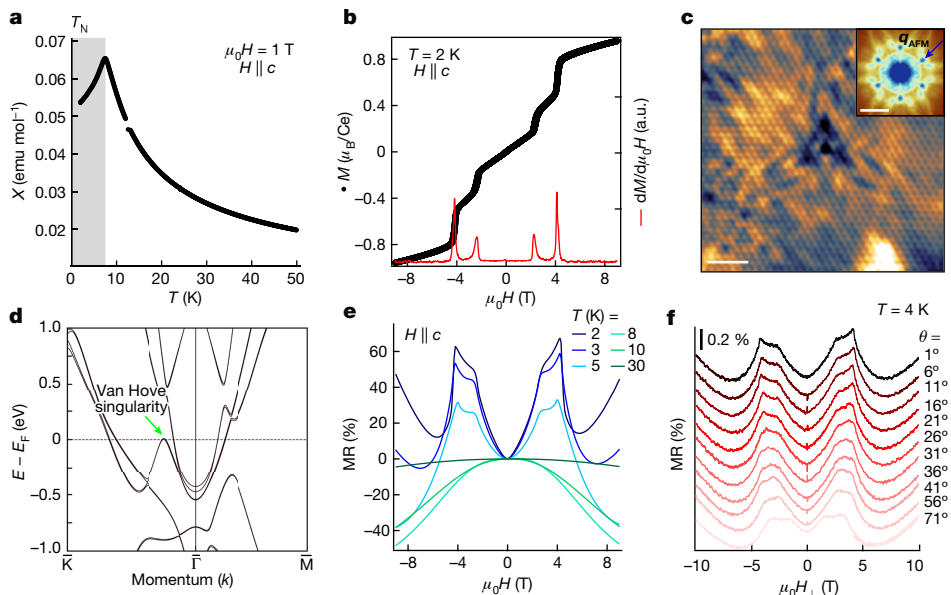


Fig. 3 | AFM ground state and metamagnetic transitions of bulk CeSiI. **a**, Temperature dependence of the magnetic susceptibility with $\mu_0H = 1\text{ T}$ and $H \parallel c$ axis. The grey region indicates the AFM phase. **b**, Field dependence of the magnetization (M) at $T = 2\text{ K}$ and $H \parallel c$ axis. **c**, STM topographic image of the CeSiI surface, displaying the hexagonal lattice of iodine atoms and a defect centred on the Si site. Standing wave oscillations around the defect appear at a wavelength that is equivalent to the magnetic ordering vector \mathbf{q}_{AFM} . Scale bar, 2 nm. Conditions: $T = 8\text{ K}$, 100 mV, 50 pA. Inset, Fourier transform of the STM topography, showing a peak at $\mathbf{q}_{\text{AFM}} \approx 0.28\text{ r.l.u.}$ (dark blue arrow) resulting from

a nesting wavevector. Scale bar, 0.3 r.l.u. **d**, Electronic band structure of CeSiI in a layered AFM ground state calculated using DFT + U (where U represents the strength of the electron–electron interaction of two electrons on the same lattice site, that is, the Hubbard U). The green arrow points to one of several critical points in the Brillouin zone responsible for the van Hove singularity in the density of states. **e**, Field dependence of the magnetoresistance (MR) at different temperatures with $H \parallel c$ axis. **f**, magnetoresistance as a function of the c axis contribution of the magnetic field ($\mu_0H_{\perp} = \mu_0H\cos\theta$) at different tilt angles θ . An angle of 0° implies $H \parallel c$ axis. r.l.u., reciprocal lattice units.

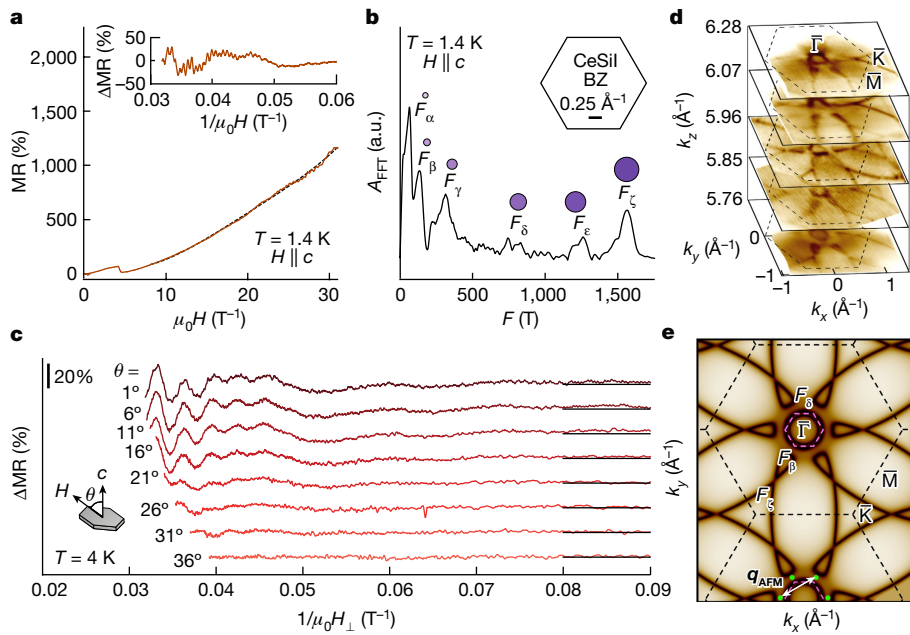


Fig. 4 | Two-dimensional electronic structure of bulk CeSiI. **a**, SdH quantum oscillations in the high magnetic field dependence of the magnetoresistance of CeSiI at $T = 1.4\text{ K}$ with $H \parallel c$ axis. Inset, oscillatory component of the magnetoresistance (ΔMR), obtained by subtracting a polynomial background (dashed line) from the raw data, as a function of $1/\mu_0H$. **b**, Fast Fourier transform (FFT) spectrum of the SdH oscillations showing six closed cyclotron orbits whose areas are drawn to scale along with the Brillouin zone (BZ) of CeSiI. **c**, Oscillatory component of the magnetoresistance versus μ_0H_{\perp} , where H_{\perp} is the c axis component of the magnetic field, at different tilt angles. **d**, k_z dependence

of the Fermi surfaces at $T = 10\text{ K}$, assuming a crystal inner potential $V_0 = 10\text{ eV}$. The photoelectron intensity was integrated over $\pm 8\text{ meV}$ around E_F . The dashed hexagons denote the Brillouin zone. **e**, Fermi surface of CeSiI in a layered AFM ground state calculated using DFT + U (see Fig. 3 for definition of U). The dashed black hexagon denotes the Brillouin zone and the pink dashed lines outline the Fermi surface. The green circles denote critical points in the Brillouin zone that manifest as a van Hove singularity in the density of states. The white arrow denotes the nesting vector \mathbf{q}_{AFM} .

produce negative magnetoresistance contributions, manifesting as distinct features (a broad kink at $\mu_0 H \approx 2.6$ T and a sharp peak at 4.2 T at $T = 2$ K) that disappear above T_N (Fig. 3e). When plotting magnetoresistance as a function of $\mu_0 H_\perp$ (Fig. 3f), where $H_\perp = H \cos\theta$ is the out-of-plane component of H and θ is the angle between H and the c axis, the metamagnetic features are sharpest when $\theta \approx 0^\circ$ and appear at nearly identical magnitudes of H_\perp for all values of θ . These data establish that the transitions are most sensitive to the c axis contribution of H and support collinear magnetic structures across the whole field range.

Electronic structure and 2D character

To investigate the Fermi surface of CeSil, we performed high-magnetic-field electrical transport measurements on bulk single crystals. At low temperature, we observe Shubnikov-de Haas (SdH) oscillations in the magnetoresistance (Fig. 4a). The frequency composition of the oscillatory component Δ MR (Fig. 4a, inset; details in Methods) reveals six frequency peaks (Fig. 4b) arising from closed cyclotron orbits in momentum space: three small (F_α, F_β and F_γ), one medium (F_δ) and two large (F_ϵ and F_ζ). The effective masses of carriers in these orbits, extracted from the temperature dependence of the oscillation amplitudes (Extended Data Fig. 8d), are comparable to that of a bare electron, suggesting either that these bands are from regions of the Fermi surface unaffected by Kondo hybridization or that the magnetic field required to observe SdH oscillations has suppressed the heavy-fermion state. Although the evolution of the Fermi surface across the magnetic phase diagram of CeSil merits further investigation, we emphasize that the observation of Kondo hybridization by STS and ARPES supports the presence of heavy bands at zero field above T_N . From the oscillation frequency of each orbit, we estimate the average Fermi wavevector \mathbf{k}_F (Methods). For the F_δ orbit, the average momentum transfer $2k_F \approx 0.3 \text{ \AA}^{-1}$ is comparable to the nesting \mathbf{q}_{AFM} vector measured by STM, implying that the AFM wavevector⁴⁴ is determined by the properties of light electrons. The angle dependence of SdH oscillations probes the dimensionality of the Fermi surface. Figure 4c displays the SdH oscillations as a function of $1/(\mu_0 H_\perp)$. With increasing θ , the oscillations remain in phase up to $\theta \approx 30^\circ$ whereas their amplitudes decrease, evidencing their dependence on the c axis contribution of H only, and thus, the quasi-2D nature of the Fermi surface.

We compare the SdH oscillations to ARPES measurements of the dispersive electronic states and identify three closed surfaces at E_F (Fig. 4d): a large hole pocket around \bar{K} , a medium electron pocket at $\bar{\Gamma}$ and a small electron pocket between $\bar{\Gamma}$ and \bar{K} . The areas enclosed by these pockets are in nominal agreement with those extracted using Onsager's relation from the F_ζ, F_δ and F_β frequencies, respectively, whereas the additional SdH peaks probably arise from magnetic breakdown between the three pockets⁴⁸. This conclusion is further supported by DFT calculations showing several bands at E_F (Fig. 4e). More broadly, DFT and ARPES demonstrate a complex electronic structure in CeSil with the number of Fermi pockets sensitive to small shifts of E_F . Importantly, however, the Fermi surface is largely unchanged along k_z (Fig. 4d), consistent with a quasi-2D electronic structure and the vdW structure of the material.

Heavy fermions in the ultra-thin limit

The quasi-2D Fermi surface suggests that Kondo hybridization will remain intact upon exfoliation. Near the 2D limit, quantum confinement is expected to strengthen electron correlations, whereas enhanced quantum fluctuations and dimensional reduction of the magnetic structure may destabilize the magnetic ground state. In this direction, the vdW nature of CeSil enables an exploration of its electrical transport properties in the ultra-thin limit. At a thickness of 15 layers (15L; Fig. 5a), $\rho(T)$ and $\rho(H)$ are nearly indistinguishable from those of the bulk (Fig. 5b). The reduced thickness, however, greatly enhances

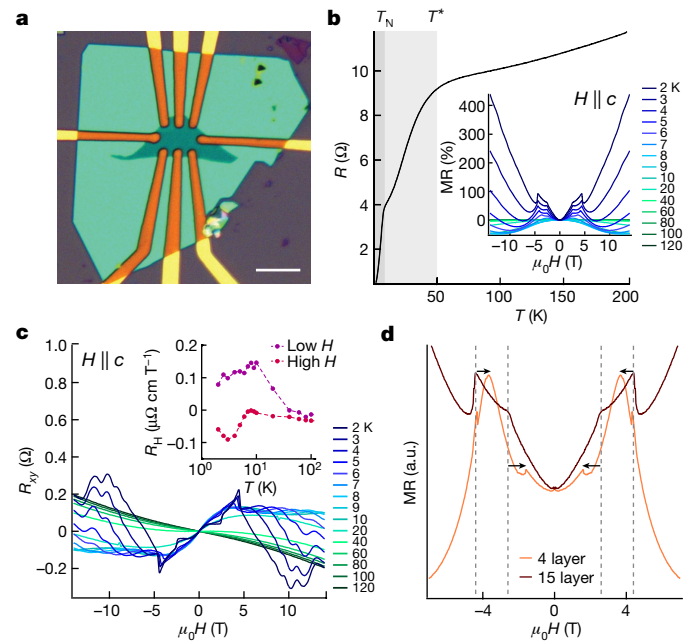


Fig. 5 | Heavy-fermion state and electrical transport in the ultra-thin regime. **a**, Optical microscopy image of an electrical transport device fabricated with a mechanically exfoliated 15L CeSil flake. Scale bar, 15 μm . **b**, Temperature dependence of the resistance (R) of the 15L flake with the darker grey region indicating the AFM ordering and the lighter grey denoting the coherence regime. Inset, Field dependence of the magnetoresistance at different temperatures with $H \parallel c$ axis. **c**, Field dependence of the Hall resistance (R_{xy}) at different temperatures with $H \parallel c$ axis. Inset, temperature dependence of the Hall coefficient $R_H = \rho_{xy}/(\mu_0 H)$ extracted from the low-field Hall data ($|\mu_0 H| \leq 0.5$ T) and high-field Hall data ($8 \leq |\mu_0 H| \leq 14$ T). **d**, Field dependence of the magnetoresistance of 4L and 15L flakes at $T = 2.5$ and 2 K, respectively, with $H \parallel c$ axis. The magnetoresistance of the 4L flake was scaled to the magnetoresistance of the 15L flake for comparison. The raw magnetoresistance data can be found in Extended Data Fig. 10d. The dashed lines mark the metamagnetic transitions for the 15L flake, and the arrows denote the shifts of the metamagnetic transitions for the 4L flake.

the Hall voltage, enabling high-resolution Hall effect measurements unfeasible in bulk crystals (Fig. 5c and Extended Data Fig. 9). Below 200 K, the Hall response is nonlinear with respect to the field, consistent with multiband transport. At high temperature ($T > 20$ K), the slope of the linear portion of the high-field Hall effect data is nearly constant, yielding an estimated net carrier density $n \approx 3.3 \times 10^{15} \text{ cm}^{-2}$ electrons per layer. At lower temperature, the Hall coefficient (R_H) in the low-field region $|\mu_0 H| \leq 0.5$ T sharply increases (Fig. 5c, inset), which we ascribe to enhanced skew scattering due to fluctuations of the Kondo-hybridized state^{44,49}. Below T_N , the temperature and field dependence of the Hall effect for CeSil is complex and requires further investigation.

On reducing the sample thickness to four layers (4L), qualitative signatures of heavy fermions remain in the transport (Extended Data Fig. 10), whereas magnetotransport (Fig. 5d) shows quantitative differences from the 15L flake. The 4L flake shows an increased resistance and a suppressed positive magnetoresistance, which is probably linked to disorder from substrate roughness, as observed for other few-layer vdW metals⁵⁰. More interestingly, both metamagnetic transitions shift to lower fields ($\mu_0 H \approx 1.6$ and 3.7 T at $T = 2.5$ K), evidencing changes to the magnetism in the ultra-thin limit. The reduction in the metamagnetic transition fields matches the changes observed under pressure (Extended Data Fig. 6), implying that exfoliation induces a small step towards the quantum critical point on the Doniach phase diagram. Although the observed magnetic changes are small for the 4L flake, we anticipate more dramatic dimensionality effects in bilayer

or monolayer CeSi₂ (ref. 26). Overall, observations of the 4L flake point to the possibility of tuning CeSi₂ towards a different ground state by exfoliation alone. Although the extreme sensitivity of thinner flakes complicates measurements in this regime, further studies will elucidate the effects of dimensionality in this heavy-fermion system.

Conclusion

Our results establish the vdW metal CeSi₂ as a 2D heavy-fermion antiferromagnet. This unique material platform allows us to probe electron correlations at microscopic length scales and explore the Doniach phase diagram using new tuning parameters enabled by exfoliation, including dimensionality, strain, symmetry breaking, gate doping and heterostructuring. Combining these tuning parameters with synthetic modifications could afford control over the balance between on-site Coulomb repulsion and hybridization, charting a path towards a programmable effective electron mass or the creation of a Kondo insulator state. Moreover, suppression of the magnetic order in CeSi₂ may lead to the emergence of superconductivity. Unexpected phenomena will undoubtedly arise. In a separate study, we demonstrated that the 2D-confined electronic structure of CeSi₂ induces anisotropic c-f hybridization, leading to the coexistence of light and heavy charge carriers.

Online content

Any methods, additional references, Nature Portfolio reporting summaries, source data, extended data, supplementary information, acknowledgements, peer review information; details of author contributions and competing interests; and statements of data and code availability are available at <https://doi.org/10.1038/s41586-023-06868-x>.

- Mathur, N. D. et al. Magnetically mediated superconductivity in heavy fermion compounds. *Nature* **394**, 39–43 (1998).
- Gegenwart, P., Si, Q. & Steglich, F. Quantum criticality in heavy-fermion metals. *Nat. Phys.* **4**, 186–197 (2008).
- Yazdani, A., da Silva Neto, E. H. & Aynajian, P. Spectroscopic imaging of strongly correlated electronic states. *Annu. Rev. Condens. Matter Phys.* **7**, 11–33 (2016).
- Löhneysen, H. V., Rosch, A., Vojta, M. & Wölfle, P. Fermi-liquid instabilities at magnetic quantum phase transitions. *Rev. Mod. Phys.* **79**, 1015–1075 (2007).
- Stewart, G. R. Heavy-fermion systems. *Rev. Mod. Phys.* **56**, 755 (1984).
- Jiao, L. et al. Chiral superconductivity in heavy-fermion metal UTe₂. *Nature* **579**, 523–527 (2020).
- Shishido, H. et al. Tuning the dimensionality of the heavy fermion compound CeIn₃. *Science* **327**, 980–983 (2010).
- Mizukami, Y. et al. Extremely strong-coupling superconductivity in artificial two-dimensional Kondo lattices. *Nat. Phys.* **7**, 849–853 (2011).
- Naritsuka, M. et al. Tuning the pairing interaction in a d-wave superconductor by paramagnons injected through interfaces. *Phys. Rev. Lett.* **120**, 187002 (2018).
- Väistö, V. et al. Artificial heavy fermions in a van der Waals heterostructure. *Nature* **599**, 582–586 (2021).
- Jang, B. G., Lee, C., Zhu, J. X. & Shim, J. H. Exploring two-dimensional van der Waals heavy-fermion material: data mining theoretical approach. *npj 2D Mater. Appl.* **6**, 80 (2022).
- Novoselov, K. S., Mishchenko, A., Carvalho, A. & Castro Neto, A. H. 2D materials and van der Waals heterostructures. *Science* **353**, aac9439 (2016).
- Fisk, Z., Sarrao, J. L., Smith, J. L. & Thompson, J. D. The physics and chemistry of heavy fermions. *Proc. Natl Acad. Sci.* **92**, 6663–6667 (1995).
- Wirth, S. & Steglich, F. Exploring heavy fermions from macroscopic to microscopic length scales. *Nat. Rev. Mater.* **1**, 16051 (2016).
- Andres, K., Graebner, J. E. & Ott, H. R. 4f-virtual-bound-state formation in CeAl₃ at low temperatures. *Phys. Rev. Lett.* **35**, 1779 (1975).
- Auerbach, A. & Levin, K. Kondo bosons and the Kondo lattice: microscopic basis for the heavy Fermi liquid. *Phys. Rev. Lett.* **57**, 877 (1986).
- Park, T. et al. Hidden magnetism and quantum criticality in the heavy fermion superconductor CeRhIn₅. *Nature* **440**, 65–68 (2006).
- Kimura, N. et al. Pressure-induced superconductivity in noncentrosymmetric heavy-fermion CeRhSi₃. *Phys. Rev. Lett.* **95**, 247004 (2005).
- Steppeke, A. et al. Ferromagnetic quantum critical point in the heavy-fermion metal YbNi₄(P_{1-x}As_x)₂. *Science* **339**, 933–936 (2013).
- Paschen, S. et al. Hall-effect evolution across a heavy-fermion quantum critical point. *Nature* **432**, 881–885 (2004).
- Monthoux, P., Pines, D. & Lonzarich, G. Superconductivity without phonons. *Nature* **450**, 1177–1183 (2007).
- Izawa, K. et al. Angular position of nodes in the superconducting gap of quasi-2D heavy-fermion superconductor CeCoIn₅. *Phys. Rev. Lett.* **87**, 057002 (2001).
- Settai, R. et al. Quasi-two-dimensional Fermi surfaces and the de Haas-van Alphen oscillation in both the normal and superconducting mixed states of CeCoIn₅. *J. Phys. Condens. Matter* **13**, L627 (2001).
- Hegger, H. et al. Pressure-induced superconductivity in quasi-2D CeRhIn₅. *Phys. Rev. Lett.* **84**, 4986 (2000).
- Li, Y. S. et al. Growth and properties of heavy fermion CeCu₂Ge₂ and CeFe₂Ge₂. *Appl. Phys. Lett.* **99**, 042507 (2011).
- Ishii, T. et al. Tuning the magnetic quantum criticality of artificial superlattices CeRhIn₅/YbRhIn₅. *Phys. Rev. Lett.* **116**, 206401 (2016).
- Devarakonda, A. et al. Clean 2D superconductivity in a bulk van der Waals superlattice. *Science* **370**, 231–237 (2020).
- Levy, P. M. & Zhang, S. Crystal-field splitting in Kondo systems. *Phys. Rev. Lett.* **62**, 78 (1989).
- Brouet, V. et al. Angle-resolved photoemission study of the evolution of band structure and charge density wave properties in RTe₃ (R = Y, La, Ce, Sm, Gd, Tb, and Dy). *Phys. Rev. B* **77**, 235104 (2008).
- Ru, N. & Fisher, I. R. Thermodynamic and transport properties of YTe₃, LaTe₃, and CeTe₃. *Phys. Rev. B* **73**, 033101 (2006).
- Ramires, A. & Lado, J. L. Emulating heavy fermions in twisted trilayer graphene. *Phys. Rev. Lett.* **127**, 026401 (2021).
- Zhao, W. et al. Gate-tunable heavy fermions in a moiré Kondo lattice. *Nature* **616**, 61–65 (2023).
- Mattausch, H. & Simon, A. Si₆, Si₁₄, and Si₂₂ rings in iodide silicides of rare earth metals. *Angew. Chem. Int. Ed.* **37**, 499–502 (1998).
- White, B. D., Thompson, J. D. & Maple, M. B. Unconventional superconductivity in heavy-fermion compounds. *Phys. C* **514**, 246–278 (2015).
- Zhang, S. et al. Electronic structure and magnetism in the layered triangular lattice compound CeAuAl₄Ge₂. *Phys. Rev. Mater.* **1**, 044404 (2017).
- de Boer, F. R. et al. CeCu₂Ge₂: magnetic order in a Kondo lattice. *J. Magn. Magn. Mater.* **63–64**, 91–94 (1987).
- Thamizhavel, A. et al. Anisotropic magnetic properties of a pressure-induced superconductor Ce₂Ni₃Ge₅. *J. Phys. Soc. Jpn.* **74**, 2843–2848 (2005).
- Kashiba, S., Maekawa, S., Takahashi, S. & Tachiki, M. Effect of crystal field on Kondo resistivity in Ce compounds. *J. Phys. Soc. Jpn.* **55**, 1341–1349 (1986).
- Seiro, S. et al. Evolution of the Kondo lattice and non-Fermi liquid excitations in a heavy-fermion metal. *Nat. Commun.* **9**, 3324 (2018).
- Aynajian, P. et al. Visualizing heavy fermions emerging in a quantum critical Kondo lattice. *Nature* **486**, 201–206 (2012).
- Patil, S. et al. ARPES view on surface and bulk hybridization phenomena in the antiferromagnetic Kondo lattice CeRh₂Si₂. *Nat. Commun.* **7**, 11029 (2016).
- Chen, Q. Y. et al. Electronic structure study of LaCoIn₅ and its comparison with CeCoIn₅. *Phys. Rev. B* **100**, 35117 (2019).
- Reinert, F. et al. Temperature dependence of the Kondo resonance and its satellites in CeCu₂Si₂. *Phys. Rev. Lett.* **87**, 106401 (2001).
- Okuma, R., Ritter, C., Nilsen, G. J. & Okada, Y. Magnetic frustration in a van der Waals metal CeSi₂. *Phys. Rev. Mater.* **5**, L121401 (2021).
- Doniach, S. The Kondo lattice and weak antiferromagnetism. *Phys. B+C* **91**, 231–234 (1977).
- Das, P. et al. Magnitude of the magnetic exchange interaction in the heavy-fermion antiferromagnet CeRhIn₅. *Phys. Rev. Lett.* **113**, 246403 (2014).
- Ali, M. N. et al. Large, non-saturating magnetoresistance in WTe₂. *Nature* **514**, 205–208 (2014).
- Falicov, L. M. & Sievert, P. R. Magnetoresistance and magnetic breakdown. *Phys. Rev. Lett.* **12**, 558 (1964).
- Fert, A. & Levy, P. M. Theory of the Hall effect in heavy-fermion compounds. *Phys. Rev. B* **36**, 1907 (1987).
- Navarro-Moratalla, E. et al. Enhanced superconductivity in atomically thin TaS₂. *Nat. Commun.* **7**, 11043 (2016).

Publisher's note Springer Nature remains neutral with regard to jurisdictional claims in published maps and institutional affiliations.

Springer Nature or its licensor (e.g. a society or other partner) holds exclusive rights to this article under a publishing agreement with the author(s) or other rightsholder(s); author self-archiving of the accepted manuscript version of this article is solely governed by the terms of such publishing agreement and applicable law.

© The Author(s), under exclusive licence to Springer Nature Limited 2024

Methods

Synthesis and structural characterization

Single crystals of CeSi₁ and LaSi₁ were synthesized following a modified published procedure³³. Because of the air-sensitive nature of the reagents and products, all manipulations of the reagents and products were performed in an inert atmosphere of nitrogen or argon. Starting materials: Ce ingot (99.8%, Thermo Scientific), La chips (99.6%, Strem), CeI₃ powder (99.9%, Thermo Scientific), LaI₃ powder (99.99%, Thermo Scientific) and Si chips (99.9999%, Strem). Commercial CeI₃ and LaI₃ were further purified by vacuum sublimation at 900 °C for 48 h. Stoichiometric amounts of Si and CeI₃ (LaI₃) were ground and mixed with a stoichiometric amount of Ce (La) pieces. A pellet of the combined reagents was pressed and then sealed in a 4–5 cm Nb tube by arc welding. The Nb ampoule was sealed in a fused silica tube under vacuum and placed in a box oven. The furnace was heated to 997 °C over 12 h, kept at this temperature for 6 d, cooled down to 700 °C with a ramp of 3 °C h⁻¹ and finally turned off. For LaSi₁ crystals, the furnace was heated to 997 °C over 12 h, kept at this temperature for 18 d and then turned off. The resulting crystals possessed a copper metallic lustre and were characterized by single-crystal X-ray diffraction using Mo K_α radiation. Single crystals of CeSi₁ and LaSi₁ were mounted using parabar oil in a nitrogen-filled glovebox. The measurements were performed on an Agilent SuperNova diffractometer. Crysali Pro software was used for data collection and reduction and absorption correction. The structures were solved in OLEX2 (ref. 51) using SHELXT⁵² and refined using SHELXL⁵³. The crystal structures are consistent with previous reports^{33,44}.

Atomic force microscopy

Single crystals of CeSi₁ were exfoliated in a nitrogen-filled glovebox using Scotch Magic tape and transferred to a 100 nm Si₃N₄/Si wafer. Before exfoliation, the wafer was heated to 350 °C for at least 24 h. Atomic force microscopy measurements of the mechanically exfoliated CeSi₁ flake were performed using a home-built cryogenic ultra-high vacuum instrument that can also serve as a scanning optical near-field microscope⁵⁴. The instrument was operated in tapping mode, in which the cantilever of a metallic tip (Rocky Mountain Nanotechnology, LLC) was vibrated near its fundamental resonance frequency. Topographic maps were recorded by scanning the sample under the tip and keeping the tip tapping amplitude constant with a Z scanner feedback loop.

Heat capacity measurements and Sommerfeld coefficient fit

Heat capacity measurements were performed on a Quantum Design Physical Property Measurement System (PPMS) DynaCool. Both single crystals and single crystals pressed into a pellet were measured. The samples were mounted with Apiezon N grease. A piece of gold foil (0.0004 inches thick) was used to encapsulate and protect them during the transfer into the PPMS. The addenda measurements were performed with the grease and the gold foil only. Data were collected at various magnetic fields between 0 and 9 T in the crystallographic c axis direction. The value of γ for non-magnetic LaSi₁ samples was extracted from the fit of the heat capacity data according to the equation:

$$\frac{C}{T} = \gamma + \beta T^2,$$

where β represents a proportionality constant for the phonon contribution to C .

Three heat capacity measurements were made of both CeSi₁ and LaSi₁, as shown in Extended Data Fig. 2a. Because of the difficulty in precisely obtaining the mass of these highly air-sensitive samples, there is some variation in the overall scale of the heat capacity. In addition, there is some slight sample dependence in the heat capacity

itself, as shown by the CeSi₁ 3 curve (light orange), which has the highest low-temperature peak but an intermediate high-temperature peak in C/T . To be systematic, we fitted all combinations of CeSi₁ and LaSi₁.

Our fit function contains three elements: a phonon background (LaSi₁, both with a fitted mass scale factor and without), a Sommerfeld function, which we approximate with a Bethe ansatz one-dimensional heat capacity solution⁵⁵ (overall scale factor fitted and T_k fixed to 74 K), and a CEF model. The CEF model was fitted in two ways: (1) a point-charge model based on the refined crystal structure of CeSi₁ calculated with PyCrystalField such that the effective point charges are fitted⁵⁶ and (2) a three-doublet model wherein we simply assume the existence of three Kramers doublets (as appropriate for Ce³⁺) and fit the two higher energies freely to the data. Two options for phonon backgrounds and two options for CEF heat capacity yielded four total fit function options. With nine different data sets to fit, this yielded 36 total fits, as shown in Extended Data Fig. 3. All fits were performed for 15 K < T < 100 K.

Clearly, not all the combinations of the data show reliable fits, particularly those that do not allow the LaSi₁ background to be scaled. If we take the fitted models with $\chi^2 < 0.001$, we find 11 Sommerfeld coefficients with a mean 0.125 J mol⁻¹ K⁻², standard deviation 0.054 J mol⁻¹ K⁻² and a range 0.031–0.217 J mol⁻¹ K⁻². These estimates show that, no matter what model is assumed, the average Sommerfeld coefficient is two orders of magnitude larger than that for typical conductors, indicating heavy-fermion behaviour.

The CEF point-charge fit included both the nearest Si and I ions, with the quantization axis along the crystallographic c axis (which is a threefold rotation axis for Ce³⁺). A point-charge model was used to calculate a ground-state doublet $|\Psi\rangle = 1.00 |\pm 5/2\rangle \pm 0.006 |\mp 1/2\rangle$. This hardly changed whether we included or excluded the I ions in the point-charge model. The point-charge model is a rough approximation, so it should be used cautiously. It predicts that the ground-state doublet is dominated by $|J_z = \pm 5/2\rangle$. Based on the fits, the first excited level is at (7.5 ± 0.5) meV for the $\chi^2 < 0.001$ set, and (9.0 ± 2.0) meV for the $\chi^2 < 0.01$ set (where the uncertainty indicates the standard deviation of the distribution of fitted levels).

Subkelvin heat capacity measurements

Low-temperature heat capacity measurements were performed using a Quantum Design PPMS dilution refrigerator insert with the samples encapsulated in Apiezon N grease for loading. Data were collected at various magnetic fields between 0 and 9 T in the crystallographic c axis direction (Extended Data Fig. 2f). The most prominent feature was a λ -anomaly at $T \approx 1$ K at low fields. We believe that this is an ordering transition of an impurity phase rather than CeSi₁, given: (1) the recovered entropy over the low-temperature anomaly was approximately 0.3 J mol⁻¹ K⁻² and was, thus, an order of magnitude lower than $R\ln(2)$, and (2) the magnitude of the heat capacity peak was strongly sample dependent.

Despite the confounding issue of the second phase, the low-field CeSi₁ heat capacity data show high heat capacity at low temperatures corresponding to many low-energy degrees of freedom, as one would expect for heavy-fermion behaviour. As the field increases, the low-temperature heat capacity decreases, corresponding to gapped excitations. This is typical behaviour of an ordered magnet in a high magnetic field.

Entropy from heat capacity

For a two-state system ($S = 1/2$), the entropy recovered from low to high temperatures should total $R\ln(2)$ per spin. This is experimentally calculated by integrating the heat capacity:

$$\Delta S = \int \frac{C}{T} dT,$$

Article

where C is the heat capacity, T is the temperature and ΔS is the entropy recovered over the integrated temperature interval. To isolate the CeSiI magnetic heat capacity, we measured and subtracted the non-magnetic LaSiI heat capacity as shown in Extended Data Fig. 2b. As noted above, there is some uncertainty in the absolute values of both the CeSiI and LaSiI heat capacities because of mass normalization. This figure has a second ‘hump’ in the C/T data with a peak at $T \approx 23$ K. When we adjusted the LaSiI mass to within a reasonable range ($\pm 20\%$), this hump persisted; therefore, it appears to be an intrinsic feature of the CeSiI magnetic heat capacity.

When we modelled this higher-temperature feature with a two-level Schottky anomaly, we got a very good match to the high-temperature heat capacity, as shown in Extended Data Fig. 2c. When we subtracted this and integrated the remaining heat capacity, we found that the heat capacity at T_N was approximately 73% of $R\ln(2)$, indicative of a potential loss of entropy due to hybridization between the local moments and conduction electrons (Extended Data Fig. 2e). The entropy reached the expected $R\ln(2)$ value at approximately 20 K. Indeed, when we did not model and subtract the 23 K Schottky mode, the 0 T Entropy between 2 and 100 K was $12.2 \text{ J mol}^{-1} \text{ K}^{-1}$, or very close to $2R\ln(2) \approx 11.53 \text{ J mol}^{-1} \text{ K}^{-1}$, the expected entropy for magnetic order combined with a crystal field level. This confirms that the ground state of Ce is a doublet.

Magnetic measurements

The magnetic properties were measured on a Quantum Design PPMS DynaCool using the vibrating-sample magnetometry option. Single crystals were sealed in a small preweighed plastic bag in a nitrogen glovebox to allow for the crystals to be weighed air-free on an analytical microbalance. To perform orientation-dependent vibrating-sample magnetometry, a 4 mm rod was placed in a quartz tube (inner diameter of 4 mm) and sealed with a 3 mm plug. To place the magnetic field parallel to the crystallographic c axis, a piece of double-sided tape with the crystals was mounted on the bottom of the 4 mm rod. For measurements in which the magnetic field was perpendicular to the crystallographic c axis, the 4 mm rod was cut into an L shape and the same piece of double-sided tape with the crystals on its side was mounted on it. The raw measured moment was corrected for the diamagnetic contribution of the sample holder by fitting the negative slope of the high field magnetization versus field data and adding the result as a temperature-independent term to the data.

Polycrystalline LaSiI powder was measured by pressing the ground powder in a polypropylene sample capsule in a nitrogen-filled glovebox. The capsule was sealed with superglue to protect the sample from air during loading of the PPMS.

Metamagnetic transition analysis

Field-induced magnetic transitions are ubiquitous in heavy-fermion materials⁵⁷. For CeSiI, the low-field ($\mu_0 H < 2.3$ T) magnetic phase is unambiguously assigned to an incommensurate AFM state, as described in a previous neutron study⁴⁴. The nature of the additional magnetization plateaus, however, merits further discussion. The larger plateau could correspond to a polarized paramagnetic state. However, across many independently prepared samples, we consistently observed the absence of magnetic saturation at 9 T. Additionally, the magnetization value observed at 9 T was much smaller than the value expected for the $m_J = 5/2$ crystal field ground state, suggesting the possibility that further metamagnetic transitions may emerge at even larger fields. One possible explanation for magnetization plateaus is a change in the ordering of the local moments leading to a fractional magnetization plateau, as reported for other triangular antiferromagnets^{58–61}. Another possibility is an intermediate paramagnetic regime, which has been observed in certain AFM heavy-fermion materials^{57,62}. Magnetization and neutron-scattering measurements at higher fields are needed to better understand the magnetic phase diagram of CeSiI.

Bulk electrical transport device fabrication

The electrical resistance of a single crystal was measured using the electrical transport option on a Quantum Design PPMS DynaCool. Single-crystal transport devices with four contacts were fabricated by mounting four gold wires (wire thickness of 0.025 mm) and a single crystal of CeSiI onto a glass coverslip with a small amount of superglue. The gold wires were placed in contact with the crystal by hand using Dupont 4929 N silver paint. The coverslip with the crystal and wires was then glued to the PPMS transport puck and the gold wires were placed in contact with the gold pads of the puck with silver paint. The sample was encapsulated in Apiezon N vacuum grease to protect it during loading of the PPMS. An a.c. current of 10 mA with a frequency ranging from 20 to 35 Hz was applied to measure the electrical transport properties from 1.8 to 300 K.

The SdH oscillations were measured using a similar fabrication process for bulk crystal devices with the cover glass mounted on a 16-pin dip socket instead of a PPMS transport puck. The devices were measured at the National High Magnetic Field Laboratory using a LakeShore Cryotronics Model 372 AC resistance bridge with a 3708 preamplifier and a rotator probe to obtain the angle dependence.

SdH oscillation analysis

The SdH oscillation frequencies were isolated by subtracting a fourth-order polynomial background and performing a fast Fourier transform. The identification of the six oscillation frequencies (Extended Data Fig. 8) was confirmed by filtering out the others and performing an inverse Fourier transform, giving results that were in good agreement with the raw data (Extended Data Fig. 8e). The areas (A_F) of the Fermi pockets were obtained from the fast Fourier transform using the Onsager relation:

$$F = \left(\frac{\phi_0}{2\pi^2} \right) A_F,$$

where F is the frequency and ϕ_0 is the magnetic flux quantum constant. We estimated the Fermi wavevector k_F from oscillations assuming a circular cross section A_F . From the temperature dependence, the effective electron mass (m^*) of the oscillations was fitted according to the following relationship⁶³:

$$\Delta R_{xx} \propto \frac{2\pi^2 k_B m^* T / \hbar e B}{\sinh(2\pi^2 k_B m^* T / \hbar e B)}.$$

The calculated effective electron masses compared to that of a bare electron indicate that the Fermi pockets originate from the lighter bands and not the heavy-fermion bands (Extended Data Fig. 8d).

STM

STM measurements were performed in a home-built instrument. Single crystals of CeSiI and LaSiI were mounted in silver epoxy in a nitrogen-filled glovebox and transported to the STM using a nitrogen suitcase to avoid exposure to air. Crystals were cleaved in situ in ultra-high vacuum conditions. The data were measured at various sample stage temperatures using electrochemically etched tungsten tips, which were calibrated using the surface state of clean Au(111) before each sample approach. Tunnelling spectroscopy data were acquired using a lock-in modulation of 2 mV at a frequency of 927 Hz. The hybridization gap in the CeSiI density of states spectrum was fitted with a spectral Fano function of the form:

$$\text{DOS}(E) = I_0 \frac{(1 + (E - E_0)/\Gamma q)^2}{1 + ((E - E_0)/\Gamma)^2},$$

which allows the Fano linewidth Γ to be extracted from this fit. The temperature dependence of Γ was used to calculate the Kondo temperature (T_K) for a single Kondo impurity using the following equation:

$$\Gamma = 2\sqrt{(\pi k_B T)^2 + 2(k_B T_K)^2}.$$

Given the difficulties associated with high-temperature STM measurements, the high-temperature data were collected through several thermal cycles, using several STM tips and on differently cleaved sample surfaces, but consistently yielded similar results to those presented in Fig. 1g.

ARPES

The CeSiL and LaSiL crystals were cleaved inside an ultra-high vacuum chamber using Kapton tape before the ARPES experiments, which were performed at the Electron Spectro-Microscopy 21-ID-1 beamline of the National Synchrotron Light Source II, USA. The beamline is equipped with a Scienta DA30 electron analyser, with base pressure approximately 2×10^{-11} mbar and various sample temperatures. The total energy and angular resolution were approximately 15 meV and approximately 0.1°, respectively.

First-principles calculations

The DFT calculations were carried out using the Quantum ESPRESSO package. We used a plane-wave basis set and the generalized gradient approximation for electron exchange and correlation. The ultrasoft⁶⁴ pseudopotential for Si and projector augmented-wave⁶⁵ pseudopotentials for Ce, La and I were obtained from PSLibrary⁶⁶ v1.0.0. The calculations were performed for CeSiL and LaSiL using the same lattice constants of $a = 4.17$ Å and $c = 11.68$ Å (ref. 33), belonging to the space group $P3\bar{m}1$. The plane-wave cutoff for the DFT calculation was set to 100 Ry for the plane-wave expansion of the wavefunctions on a $\bar{\Gamma}$ -centred k grid of size $16 \times 16 \times 4$. For LaSiL, the non-spin-polarized calculations used scalar-relativistic pseudopotentials. For CeSiL, spin-orbit coupling and non-collinear magnetic interactions were taken into account using two-spinor Kohn–Sham wavefunctions. Additionally, an on-site Coulomb energy $U = 6.0$ eV was applied for CeSiL within the rotationally invariant formulation⁶⁷ using the Löwdin-orthogonalized atomic 4f pseudo-wavefunctions of Ce as the localized basis set for the Hubbard manifold. The self-consistent DFT calculation converged to an AFM Ising configuration in which the spins of Ce above and below the silicene-like layer in the unit cell were polarized in opposite directions.

For both CeSiL and LaSiL, to calculate the Fermi surface on a finer k grid, tight-binding models in the basis sets of maximally localized Wannier functions were constructed using Wannier90 with the $Si p_z$, $Si sp^2$, $I p$ and $La/Ce 4f$ and $5d$ orbitals as initial projections. The Wannier functions were interpolated onto a k grid of size $2,700 \times 2,700$. The spectral function on the k_{xy} plane at the Fermi level was plotted on a log scale in Fig. 4e. To calculate the magnetic exchange interaction for CeSiL, we used the magnetic force theorem^{68,69} to map the tight-binding Wannier Hamiltonian onto a classical Heisenberg model using TB2J (ref. 70), using the convention that a positive value of J corresponds to ferromagnetic exchange interaction. We found that for the in-plane exchange interactions, the nearest-neighbour interaction $J_{NN} = -0.1$ meV and the next-nearest-neighbour exchange interaction $J_{NNN} = +0.01$ meV. Moreover, the interlayer magnetic exchange interaction $J_{IL} = 0.000 - 0.001$ meV. Here, J_{NN} corresponds to Ce ions vertically aligned across the silicene layer ($d_{Ce-Ce} = 4.03$ Å), whereas J_{NNN} corresponds to Ce ions horizontally displaced within the triangular layer ($d_{Ce-Ce} = 4.17$ Å). We see that these calculations yield an estimated $|J_{NN}/J_{IL}| > 100$, whereas experimental values for quasi-2D intermetallic heavy-fermion materials are typically near 10^{46} , indicating substantial exchange anisotropy in CeSiL.

Tunnel diode oscillator fabrication and pressure experimentation

A tunnel diode oscillator circuit was used to detect changes in the sample properties under pressure. The measurement set-up consisted of an LC tank circuit, which maintained a resonant frequency when the tunnel diode was tuned with an appropriate bias. The sample was placed inside a small, copper coil (an inductor approximately 1 mm long × 0.5 mm in diameter), which was wound to match the size of the crystal to maximize the filling factor. This allowed the measured circuit frequency to be sensitive to both changes in the skin depth and the magnetization, which shifted the inductance of the circuit. The coil and crystal were small enough to fit into the sample volume of a piston cylinder pressure cell with Daphne oil. This allowed us to track changes in sample behaviour as a function of pressure, temperature and field.

2D device fabrication and electrical transport

CeSiL crystals were mechanically exfoliated onto a Si/SiO₂ wafer inside an Ar glovebox with less than 0.1 ppm O₂ and H₂O. Before exfoliation, the substrate was heated on a hot plate at 300 °C for more than 24 h to remove any water from the surface. Flakes were identified by optical contrast. We used a previously reported high-resolution stencil mask technique to fabricate the devices⁷¹. This process uses neither solvents nor polymers, which helps to preserve the flakes. In addition, it can be done air-free inside the glovebox. Stencil masks were fabricated from Si₃N₄ (500 nm)/Si (300 μm)/Si₃N₄ (500 nm) wafers. A combination of photolithography, reactive ion etching and wet etching (with a potassium hydroxide solution) was used to create 200 and 500 μm square windows of Si₃N₄. The desired patterns of devices were written with photolithography on the windows and reactive ion etching was used to remove the Si₃N₄ mask. We aligned and placed the prefabricated stencil mask onto pre-identified flakes with a micropositioner. A small amount of vacuum grease (Apiezon H) was used to glue the mask to the substrate. We deposited Au metal as electrical contacts, and the device was covered with a flake of hexagonal boron nitride (thickness 20 to 40 nm) to provide extra protection from degradation. The final device was cut, mounted on a 16-pin chip carrier and wire bonded inside the glovebox. The chip carrier was covered with glass and loaded into a cryostat for the electrical measurements. The electrical transport measurements were performed in a Quantum PPMS whereas the magnetoresistance was measured with a lock-in amplifier. Note that similar Hall effect measurements in three-dimensional heavy-fermion systems often require sophisticated focused ion-beam micromachining^{72,73}; here, the ability to reduce thickness with exfoliation alone provides a simple method for studying the Hall effect in Kondo-lattice materials.

Data availability

The data that support the findings of this study are present in the paper and its Extended Data. Further data are available from the corresponding authors upon request.

51. Dolomanov, O. V., Bourhis, L. J., Gildea, R. J., Howard, J. A. K. & Puschmann, H. H. OLEX2: a complete structure solution, refinement and analysis program. *J. Appl. Crystallogr.* **42**, 339–341 (2009).
52. Sheldrick, G. M., IUCr. SHELXT – Integrated space-group and crystal-structure determination. *Acta Cryst. A* **71**, 3–8 (2015).
53. Sheldrick, G. M., IUCr. Crystal structure refinement with SHELXL. *Acta Cryst. C* **71**, 3–8 (2015).
54. Stinson, H. T. et al. Imaging the nanoscale phase separation in vanadium dioxide thin films at terahertz frequencies. *Nat. Commun.* **9**, 3604 (2018).
55. Desgranges, H.-U. & Schotte, K. D. Specific heat of the Kondo model. *Phys. Lett. A* **91**, 240–242 (1982).
56. Scheie, A. PyCrystalField: software for calculation, analysis and fitting of crystal electric field Hamiltonians. *J. Appl. Crystallogr.* **54**, 356–362 (2021).
57. Aoki, D., Knafo, W. & Sheikin, I. Heavy fermions in a high magnetic field. *C. R. Phys.* **14**, 53–77 (2013).
58. Kitazawa, H., Eguchi, S. & Kido, G. Metamagnetic transition in geometrically frustrated system TbPd_{1-x}Ni_xAl. *Phys. B* **359–361**, 223–225 (2005).

Article

59. Cable, J. W., Wilkinson, M. K., Wollan, E. O. & Koehler, W. C. Neutron diffraction investigation of the magnetic order in Mn₂. *Phys. Rev.* **125**, 1860 (1962).
60. Kurumaji, T. et al. Magnetic-field induced competition of two multiferroic orders in a triangular-lattice helimagnet Mn₂. *Phys. Rev. Lett.* **106**, 167206 (2011).
61. Kurumaji, T. et al. Magnetoelectric responses induced by domain rearrangement and spin structural change in triangular-lattice helimagnets Ni₂ and Co₂. *Phys. Rev. B* **87**, 014429 (2013).
62. Aoki, D. et al. Decoupling between field-instabilities of antiferromagnetism and pseudo-magnetism in Rh-doped CeRu₂Si₂ Kondo lattice. *J. Phys. Soc. Jpn* **81**, 034711 (2012).
63. An, L. et al. Magnetoresistance and Shubnikov-de Haas oscillations in layered Nb_xSiTe_y thin flakes. *Phys. Rev. B* **97**, 235133 (2018).
64. Rappe, A. M., Rabe, K. M., Kaxiras, E. & Joannopoulos, J. D. Optimized pseudopotentials. *Phys. Rev. B* **41**, 1227 (1990).
65. Kresse, G. & Joubert, D. From ultrasoft pseudopotentials to the projector augmented-wave method. *Phys. Rev. B* **59**, 1758 (1999).
66. Dal Corso, A. Pseudopotentials periodic table: from H to Pu. *Comput. Mater. Sci.* **95**, 337–350 (2014).
67. Anisimov, V. I., Aryasetiawan, F. & Liechtenstein, A. I. First-principles calculations of the electronic structure and spectra of strongly correlated systems: the LDA+U method. *J. Phys. Condens. Matter* **9**, 767 (1997).
68. Liechtenstein, A. I., Katsnelson, M. I., Antropov, V. P. & Gubanov, V. A. Local spin density functional approach to the theory of exchange interactions in ferromagnetic metals and alloys. *J. Magn. Magn. Mater.* **67**, 65–74 (1987).
69. Liechtenstein, A. I., Katsnelson, M. I. & Gubanov, V. A. Exchange interactions and spin-wave stiffness in ferromagnetic metals. *J. Phys. F: Met. Phys.* **14**, L125 (1984).
70. He, X., Helbig, N., Verstraete, M. J. & Bousquet, E. TB2J: a Python package for computing magnetic interaction parameters. *Comput. Phys. Commun.* **264**, 107938 (2021).
71. Zhao, S. Y. F. et al. Sign-reversing Hall effect in atomically thin high-temperature Bi₂Sr_{1-x}CaCu_{2-x}O_{6.5} superconductors. *Phys. Rev. Lett.* **122**, 247001 (2019).
72. Moll, P. J. W. et al. Field-induced density wave in the heavy-fermion compound CeRhIn₅. *Nat. Commun.* **6**, 6663 (2015).
73. Bachmann, M. D. et al. Spatial control of heavy-fermion superconductivity in CeIrIn₅. *Science* **366**, 221–226 (2019).
- Sciences, Materials Sciences and Engineering Division. The specific heat analysis used resources at the Spallation Neutron Source, a DOE Office of Science User Facility operated by the Oak Ridge National Laboratory. The PPMS used to perform vibrating-sample magnetometry, heat capacity and electrical transport measurements was purchased with financial support from the NSF through a supplement to award DMR-1751949. STM equipment support was provided by the Air Force Office of Scientific Research via grant FA9550-21-1-037. Electrical transport measurements of low-dimensional samples were supported by the NSF (DMR-2105048). Nano-imaging experiments and theoretical modelling were supported as part of Programmable Quantum Materials, an Energy Frontier Research Center funded by the DOE, Office of Science, Basic Energy Sciences (Award DE-SC0019443). The theory calculations by O.E., P.T. and C.-S.O. were supported by an ERC synergy grant (FASTCORR, project 854843), the Swedish Research Council, eSSENCE, STandUPP and the Wallenberg Initiative Materials Science for Sustainability (WISE) funded by the Knut and Alice Wallenberg Foundation (KAW), the Swedish National Infrastructure for Computing, Grupos Consolidados (IT1453-22), and the German Research Foundation through the Cluster of Excellence CUI: Advanced Imaging of Matter (EXC 2056, project ID 390715994) and Project SFB-925 Light-induced Dynamics and Control of Correlated Quantum Systems (Project 170620586). V.A.P. is supported by the NSF Graduate Research Fellowship Program (NSF GRFP 2019279091). A.D. acknowledges support from the Simons Foundation Society of Fellows programme (Grant No. 855186). We acknowledge the use of facilities and instrumentation supported by the NSF through the Columbia University, Materials Research Science and Engineering Center (Grant No. DMR-2011738). The Flatiron Institute is a division of the Simons Foundation. We acknowledge support from the Max Planck–New York City Center for Non-Equilibrium Quantum Phenomena.

Author contributions V.A.P., S.T., A.N.P. and X.R. conceptualized the project. V.A.P., D.G.C. and E.M. were responsible for synthesis and methodology. V.A.P. and M.E.Z. were responsible for magnetometry. V.A.P., A.S. and A.F.M. were responsible for heat capacity measurements. S.T. and M.T. were responsible for scanning tunnelling microscopy. V.A.P. was responsible for bulk electrical transport. D.R.N. and X.-Y.Z. were responsible for spectroscopy. V.A.P., A.D., C.R.D. and D.G. were responsible for high-magnetic-field electrical transport measurements. V.A.P., M.E.Z. and D.G. were responsible for tunnel diode oscillator pressure experiments. M.R., X.C. and P.K. were responsible for 2D electrical transport. R.A.V., R.J., S.X. and D.N.B. were responsible for atomic force microscopy. V.A.P., A.J., M.R., M.L.F. and X.C. were responsible for exfoliation. C.S.O., P.T., O.E., A.J.M. and A.R. conducted the first-principles calculations. A.K.K., T.V., T.Y. and E.V. were responsible for ARPES. V.A.P., S.T., M.R., A.D., A.K.K., C.S.O., A.J.M., M.E.Z., A.N.P. and X.R. wrote the paper. A.N.P. and X.R. supervised.

Competing interests The authors declare no competing interests.

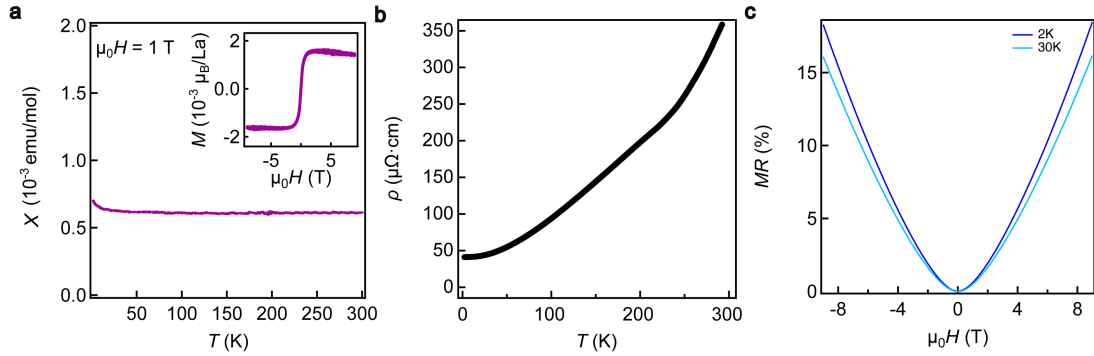
Additional information

Correspondence and requests for materials should be addressed to Angel Rubio, Michael E. Ziebel, Andrew J. Millis, Abhay N. Pasupathy or Xavier Roy.

Peer review information Nature thanks the anonymous reviewers for their contribution to the peer review of this work.

Reprints and permissions information is available at <http://www.nature.com/reprints>.

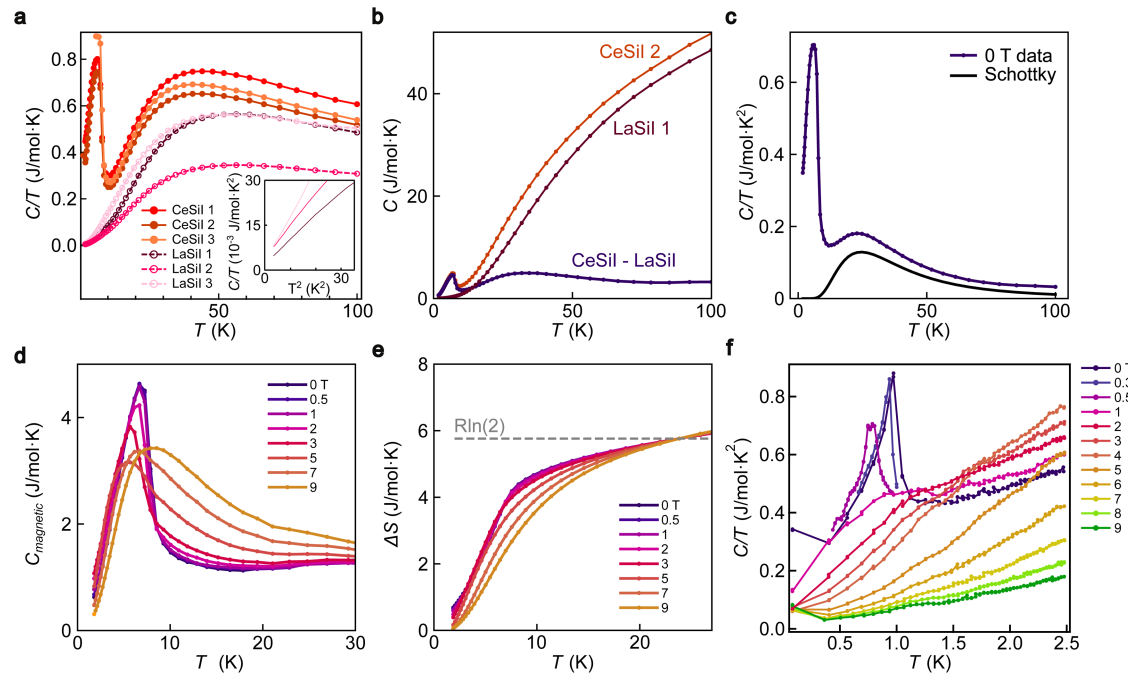
Acknowledgements Research on 2D heavy-fermion materials was primarily supported by the US Department of Energy (DOE), Office of Science, Basic Energy Science, under award DE-SC0023406. ARPES measurements were performed at Beamline 21-ID-1 of the National Synchrotron Light Source II, a DOE Office of Science User Facility operated for the DOE Office of Science by Brookhaven National Laboratory (Contract No. DE-SC0012704). We thank C. Petrovic and Z. Hu for their help with the sample mounting for ARPES. High-magnetic-field transport and tunnel diode oscillator measurements were performed at the National High Magnetic Field Laboratory, which is supported by the National Science Foundation (NSF; Cooperative Agreement No. DMR-1644779) and the State of Florida. Subkelvin specific heat capacity measurements (A.F.M.) were supported by the DOE, Office of Science, Basic Energy



Extended Data Fig. 1 | Magnetism and electrical transport of LaSil.

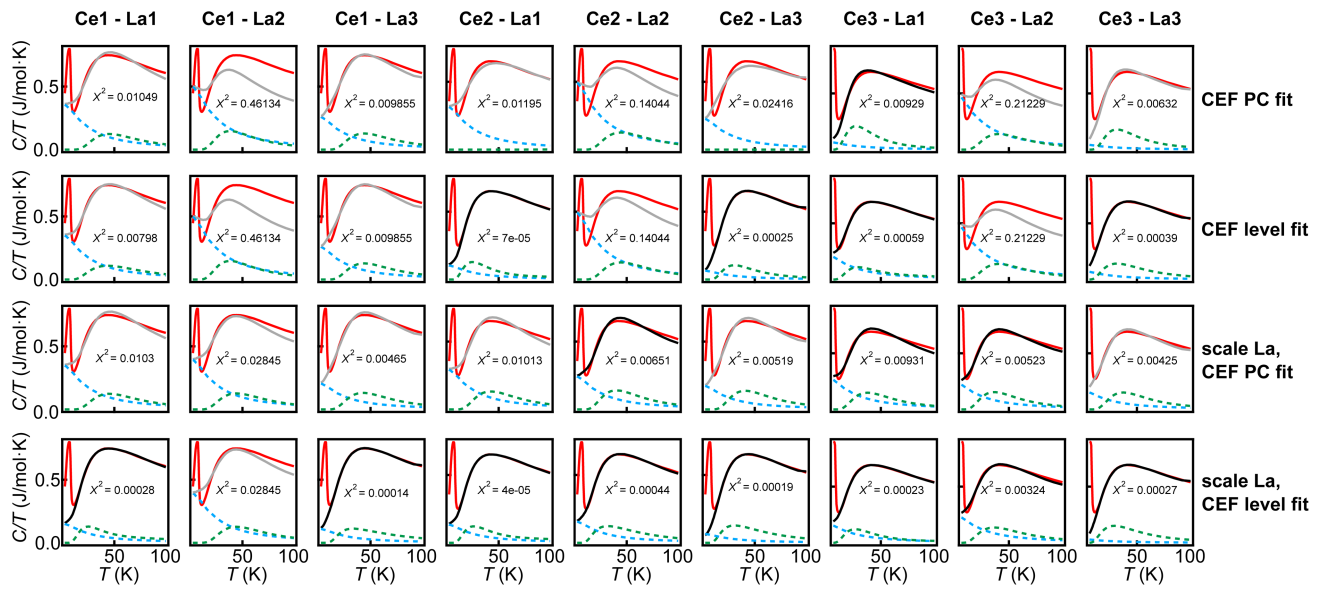
a, Temperature dependence of the magnetic susceptibility measured with an applied magnetic field of 1 T. The magnetic susceptibility of LaSil is essentially temperature independent over the whole temperature range with no magnetic transition, and ca. one order of magnitude smaller than that of CeSil. This is consistent with a non-magnetic system with a small amount of a

ferromagnetic impurity, presumably iron or iron oxide. Inset: the field dependence of the magnetization at $T = 2 \text{ K}$, showing a clear ferromagnetic response, verifies the presence of a ferromagnetic impurity. Assuming the impurity is Fe, we can estimate the amount in the sample to be $-1.83 \mu\text{g}$ (-0.01 wt\%). **b**, Temperature dependence of the resistivity of LaSil at zero magnetic field. **c**, Magnetoresistance of LaSil at $T = 2$ and 30 K .



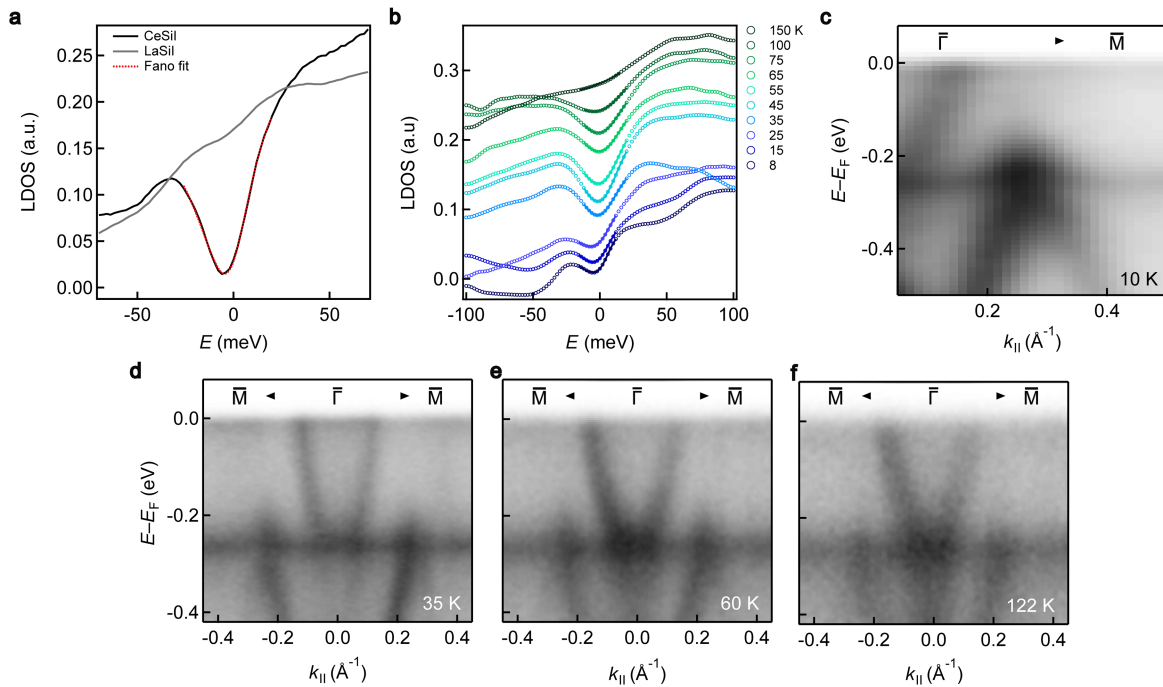
Extended Data Fig. 2 | Magnetic heat capacity, entropy, and dilution refrigerator heat capacity. **a**, Heat capacity of multiple samples of CeSil and LaSil. Inset: C/T vs T^2 fit for the LaSil samples. **b**, Temperature dependence of the heat capacity of CeSil and LaSil. The magnetic heat capacity of CeSil is estimated by subtracting C_{LaSil} from C_{CeSil} ($C_{\text{mag}} = C_{\text{CeSil}} - C_{\text{LaSil}}$). **c**, Temperature dependence of the magnetic heat capacity and a fitted Schottky anomaly corresponding to a low-lying crystal field level. **d**, Temperature dependence

of the magnetic heat capacity at different magnetic fields with the Schottky contribution subtracted. **e**, Temperature dependence of the entropy calculated from the heat capacity data with the zero-field Schottky contribution subtracted. The entropy associated with the magnetic transition is close to the expected value $R \ln(2)$ for a doublet ground state. **f**, Low temperature dependence of C/T measured at different magnetic fields.



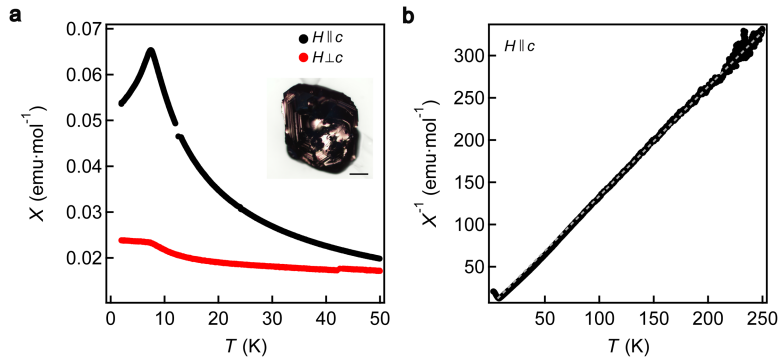
Extended Data Fig. 3 | Heat Capacity Fits for Sommerfeld Coefficient of CeSil. C/T of CeSil (red) and fitted model (black/grey) for $15 < T < 100$ K. The Bethe Ansatz Sommerfeld and CEF contributions to the total model are shown

by blue and green dashed curves, respectively. Grey lines are fits with $\chi^2 > 0.01$, and thick black lines are fits with $\chi^2 < 0.01$.



Extended Data Fig. 4 | Temperature dependence of STS and ARPES, and comparison to LaSiL. **a**, Scanning tunneling spectra of CeSiL and LaSiL measured at $T = 8$ K, 300 mV, and 200 pA. The Fano fit for CeSiL is shown in red. **b**, The temperature dependence of the spectra of CeSiL with the smaller data set

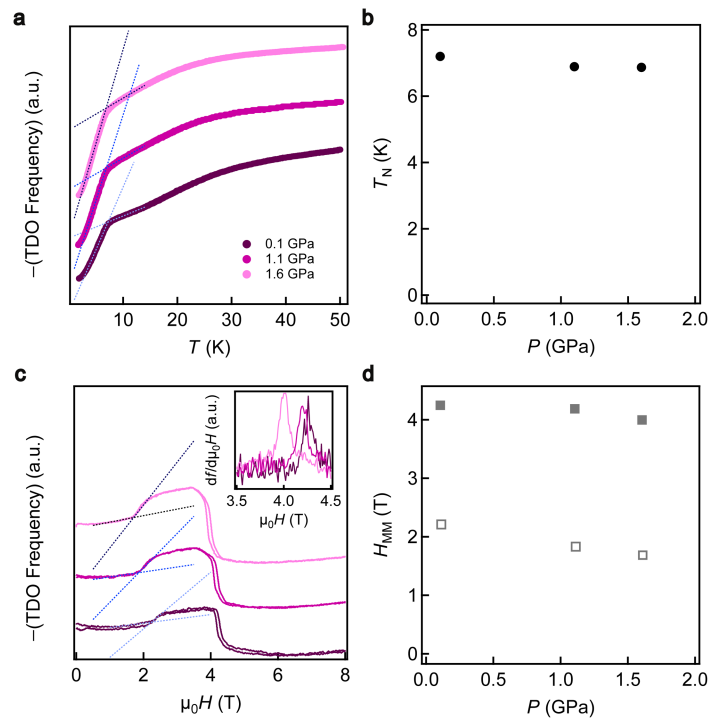
shown in Fig. 1e. **c**, Magnified ARPES spectrum from the red box in Fig. 2a along the $\bar{\Gamma}$ – \bar{M} path showing the hybridization between the itinerant states and the f bands. (Conditions: $T = 10$ K, photon energy of 135 eV). ARPES spectra of CeSiL at **d**, 35 K, **e**, 60 K, and **f**, 122 K taken at a photon energy of 121 eV.



Extended Data Fig. 5 | Orientation dependent magnetism of CeSiI.

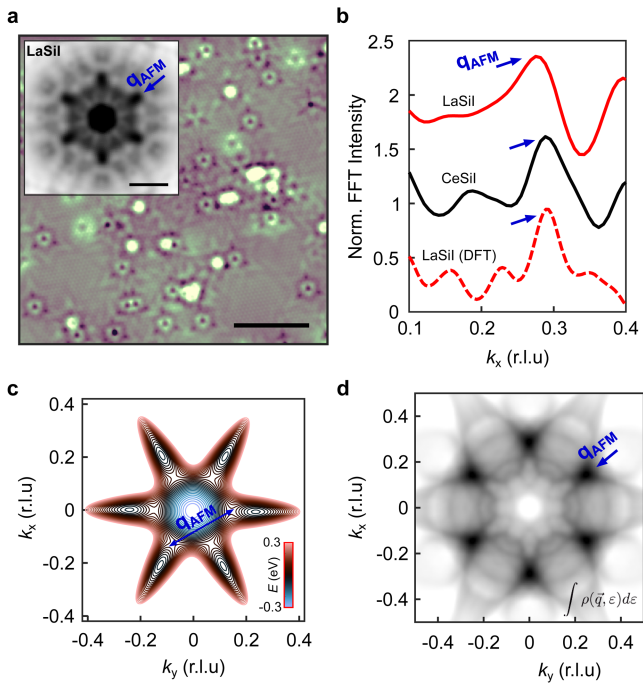
Temperature dependence of the magnetic susceptibility with an applied magnetic field of 1 T with the field parallel and perpendicular to the c-axis. The inset shows an optical microscope image of a CeSiI crystal with a scale bar of

100 μm . **b**, Curie-Weiss curve with a field of 1 T parallel to the crystallographic c-axis and the grey dashed line representing the Curie-Weiss fit with $C = 0.771 \text{ emu K mol}^{-1}$ ($\mu_{\text{eff}} = 2.48$) and $\theta = -3 \text{ K}$. The expected value of C for Ce^{3+} is $0.804 \text{ emu K mol}^{-1}$ ($\mu_{\text{eff}} = 2.54$).



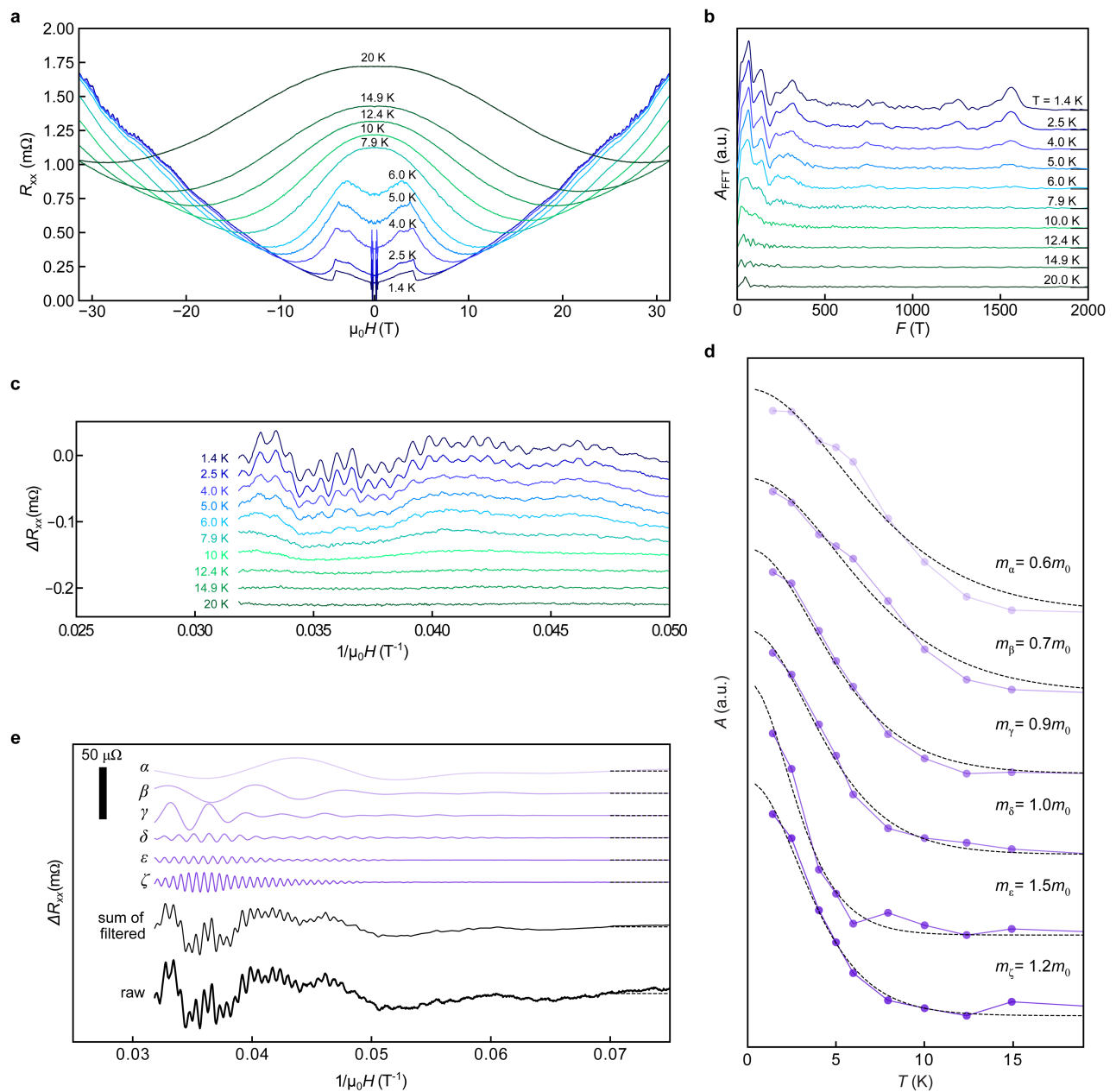
Extended Data Fig. 6 | Pressure dependence of magnetism and the metamagnetic transitions in tunnel diode oscillator devices. **a**, The inverse frequency of the tunnel diode oscillator (TDO) as a function of temperature at different pressures. The fits to extract the broad antiferromagnetic peak are shown as dotted blue lines. **b**, Pressure dependence of T_N obtained from the fits in panel (a). **c**, Magnetic field dependence of the inverse TDO frequency at

$T = 1.8$ K. The blue dotted lines denote the fit for the first metamagnetic transition and the inset displays the derivative to extract the field for the second metamagnetic transition. **d**, Pressure dependence of the field for the first (open grey square) and second (closed grey square) metamagnetic transitions (H_{MM}). The first metamagnetic transition shows a slightly greater pressure dependence than the second.



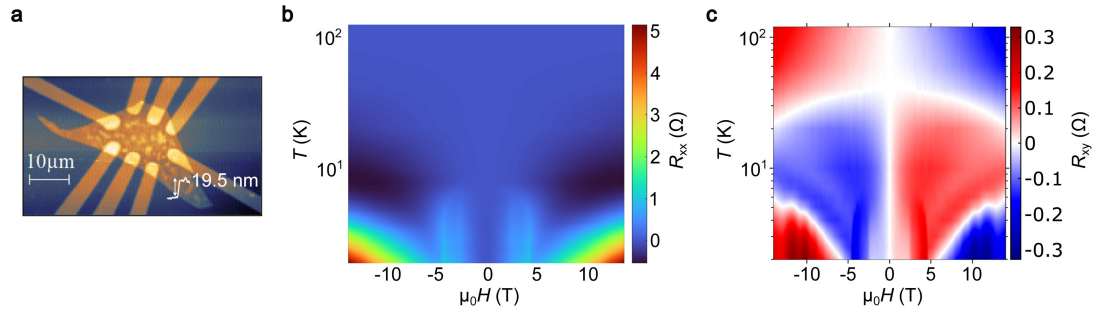
Extended Data Fig. 7 | STM analysis of LaSil and nesting vector. **a**, STM topographic image of LaSil, displaying the hexagonal lattice of iodine atoms and surface defects. Scale bar: 8 nm. Conditions: $T = 8\text{ K}$, 100 mV, 50 pA. Inset: Fourier transform of the STM topography, showing the same peak at $\mathbf{q}_{\text{AFM}} \sim -0.28\text{ r.l.u.}$ (dark blue arrow, r.l.u. = reciprocal lattice units) as CeSil (Fig. 3c), which results from a nesting wavevector. Scale bar: 0.25 r.l.u. **b**, Line cut of the Fourier transform along k_x showing a peak in intensity at \mathbf{q}_{AFM} (blue arrows) for LaSil and CeSil and in the DFT calculated spectrum of LaSil. **c**, Contour plot of the calculated DFT band of LaSil. The blue arrow indicates the \mathbf{q}_{AFM} nesting wavevector between two critical points in the Brillouin zone. **d**, Simulation of the LaSil STM Fourier space displaying a peak in intensity at the \mathbf{q}_{AFM} nesting wavevector.

Article



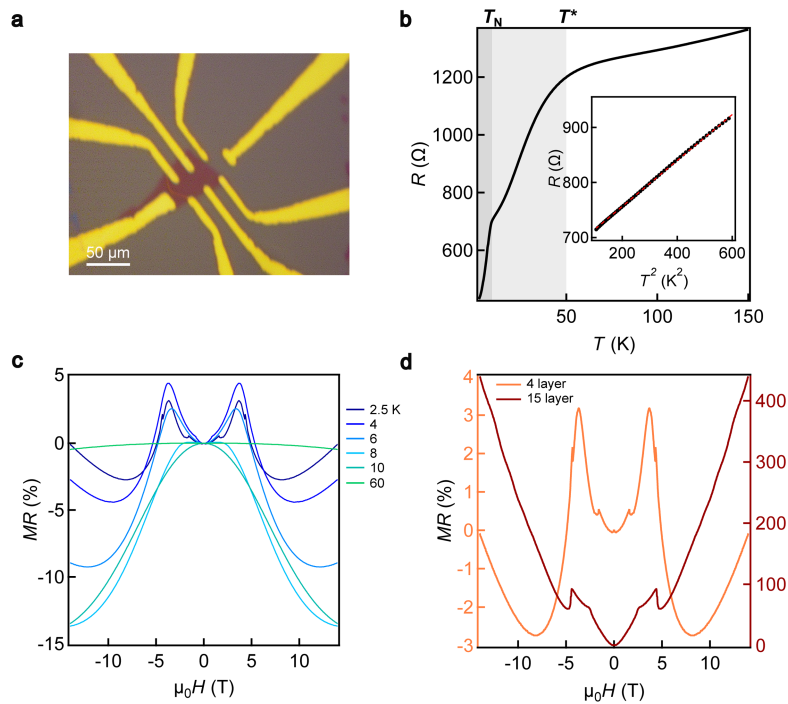
Extended Data Fig. 8 | Analysis of the CeSiI SdH oscillations. **a**, High field magnetoresistance of CeSiI at different temperatures. **b**, Amplitude of the Fast Fourier transform (A_{FFT}) versus the frequency (F) at different temperatures. **c**, Oscillatory component (ΔR_{xx}) obtained by subtracting a polynomial background from the magnetoresistance. **d**, Temperature dependence of the

SdH oscillation amplitudes (A) with the effective mass for each frequency peak displayed with respect to the mass of a bare electron (m_0). The dashed lines are the fits used to calculate the effective electron masses. **e**, Filtered oscillations compared to the raw data.



Extended Data Fig. 9 | Atomic force microscopy image and additional electrical characterization for the 15 L device. **a**, Atomic force microscopy image of a 15 L device. **b**, 2D plot of the longitudinal resistance (R_{xx}) as a

function of the temperature and applied magnetic field. **c**, 2D plot of the Hall resistivity (R_{xy}) as a function of the temperature and applied magnetic field.



Extended Data Fig. 10 | Optical microscope image and additional electrical characterization for the 4 L device. **a**, Optical microscope image of the 4 L device. **b**, Temperature dependence of the resistivity. The overall behavior is qualitatively similar to that of the bulk crystal, with a broad transition around

50 K and a sharp kink at 7.5 K resulting from the AFM ordering. Inset: R versus T^2 . The linear fit (red line) denotes a Fermi liquid state. **c**, Field dependence of the magnetoresistance at different temperatures with $H \parallel c$ -axis. **d**, Field dependence of the magnetoresistance of the 4 L and 15 L flakes.